Structure, Optics, Visible Light and Photocatalytic Activity of Pure and Pd Doped Tungsten Trioxide Nanoparticles Synthetized by the Microwave Irradiation Method

D. Madhan[1*], M. Sangeetha[2] and A. Panneerselvam[3]

[1]*Assistant Professor of Physics, Velammal College of Engineering and Technology, Madurai-625009, Tamilnadu, India*
[2]*Assistant Professor of Chemistry, E. M. G Yadava Women's College, Madurai-625014, Tamilnadu, India*
[3]*Associate Professor of Physics, Vivekananda College for Women, Namakkal-637205, Tamilnadu, India*
*Corresponding author: madhan14d@gmail.com

Received 15/10/2022; accepted 20/01/2023
https://doi.org/10.4152/pea.2024420303

Abstract
In view of enhanced Pc applications, doped materials have drawn much attention. The present work focused on synthesizing pure and Pd doped WO_3 Np, which were used as Pc for MB and RhB aqueous solutions discoloration, under VL, by a unique MWI technique. XRD and TEM studies revealed that Pd dopant did not influence WO_3 samples structure and morphology, since they had mono-dispersed spherical forms, with an average diameter of about 50-30 nm. Optical spectra showed a red shift in the absorption edges, with an increase in Ct of Pd from 0 to 10 wt%, which indicates the decrease in E_g of WO_3 with Pd doping. E_g was calculated as 3.02, 2.84 and 2.73 eV, for pure and Pd (5 and 10 wt%) doped WO_3 samples, respectively. Pc intensity of Pd doped WO_3 was significantly higher than that of the pure one. This was due to the recombination of photo-excited electrons and holes. Pc activities of pure and Pd doped WO_3 samples were analyzed based on their ability to degrade MB and RhB dyes under VL. Pd doped WO_3 showed better Pc degradation, due to an increase in SA, and a decrease in E_g and O vacancies.

Keywords: MWI; Pc; Pd; TEM; WO_3; VL; XRD.

Introduction•

Sc Np draw keen interest nowadays, for basic research and technical applications, due to their optical, electronic and structural properties that are size dependent and have quantum confined effects. Currently, nanotechnology and Np play significant roles in many fields, with environmental, biological and energy storage devices applications [1, 2].

In Pc, organic pollutants are degraded by the oxidative species generated upon photoexcitation. Some nano Pc, such as SnO_2, TiO_2, WO_3, ZnO, CuO and ZnO_2, have been prepared to achieve this effect. There has been wide interest in the synthesis of transition metal oxides Sc with various morphological structures and

• The abbreviations and symbols definition lists are in pages 200-201.

properties [3]. TiO_2 is one of the generally studied Pc, since it is not toxic and is highly photostable [4, 5]. However, so far, Pc still are not very efficient, which draws them away from practical applications. It was mentioned that their efficiency can be improved by controllable modulation of light generation and behavior of photo generated charge carriers. This can be done through different design concepts, such as modulation of crystallographic facets and morphology, doping, sensitization, surface treatment, and combination with other Sc and noble metals [6-8]. Pc can be used to convert sunlight into chemical energy, which could achieve various purposes, such as H fuel production through water splitting, refinement of several aqueous media and green synthesis of different chemicals [9].

Due to the development of industrialization and urbanization, water contamination has dangerously grown. Water pollution has brought diseases to humans, such as cholera, diarrhea and hepatitis. Organic dyes are also a major constituent in polluted water discharged from textile, food and cosmetic industries. Among these organic dyes, MB is considered one of the most toxic, since it causes eye irritation, vomiting, nausea and confusion [10]. Thus, it is important to discover a suitable material able to remove this harmful dye from contaminated water [11, 12]. Unrefined dyes in textile effluents are a serious ecological problem [13]. Hence, dispose of pollutants from wastewaters is essential for the environment [14]. Metal oxides Sc with sensible E_g show lower light-harvesting ability in VL. Hence, Sc grouping with different band E_g is one of the approaches to the synthesis of high active and stable Pc. Among the different metal oxides Pc Sc, WO_3 is one of the best, since it is extraordinary stable, has good electron transport properties and high photoactivity, with no photo-corrosion [15]. WO_3 is an auspicious n-type Sc with admirable electro, photo and gasochromic properties. It has been extensively used in different practical applications, including gas and temperature sensing catalysis, electrochromic windows and displays, flat panels and solar energy devices [16, 17]. WO_3 Np could be a potential catalyst for the manufacture of solar response Pc with absorption in the visible range [18].

There are many dopants and additives able to develop the Pc performance of WO_3. WO_3 chemical doping with metallic Pd [19], Cu [20] and Sn [21] changes Sc electronic structures and surface properties, thus extending their VL absorption. Pd-doped metal oxide Sc have stronger Pc performance and gas-sensing properties than those of the pure ones [22-26]. This improved Pc performance is mainly due to E_g modification upon doping, according to Moss-Burstein effect, which is derived from the Pauli exclusion principle [27-29]. Besides, Pc efficiency of Sc can be improved by reducing their particle size [30]. Among various metals, Pd is an efficient dopant for enhancing Pc performance of WO_3, since it is able to improve SA and separation of photo generated charge carriers.

Hence, in the present study, Pd was chosen as a dopant, for enhancing WO_3 structural and optical properties and Pc activities.

Eu^{3+} doped WO_3 Np were successfully prepared by Pechini's modified method. Pc activities of the Np were evaluated by their RhB decomposition. The results indicated that Eu^{3+} doped WO_3 Np had high Pc activity [31]. $WO_3.H_2O$ Np were prepared by MWI method [32].

Herein, WO_3 Np were directly prepared during MWI process. Many techniques have been developed for the synthesis of WO_3 Np, such as hydrothermal route [33], surfactant mediated [34], sol gel [35], chemical co-precipitation [36],

acidification [37] and electrodeposition methods [38]. MWI was also effectively used to modify metal oxides Sc morphologies, surfaces and particle sizes, which have wide effects on Pc properties.
In the present study, a novel MWI technique was used to synthesize pure and Pd doped WO_3 Np. To the best of our knowledge, this is the first study of the MWI method on pure and Pd-doped WO_3 Np structural and optical properties and Pc activity.
In addition, this technique has drawn much attention, due to its higher simplicity, effectiveness, large scale production [39], low-cost route to synthesis and swiftness (about 10 min) than those of other preparation techniques.

Experimental procedure

Preparation of pure and Pd doped WO_3 Np

Chemicals and reagents

The employed chemicals, such as H_2WO_4 (99.97%) and $PdCl_2.2H_2O$ (99.97%) were purchased from Sigma-Aldrich. Ethanol, NaOH, HCl, MB and RhB dyes (99.99%) were purchased from Merck. All the above chemicals were of analytical grade, and were used without any further purification.
H_2WO_4 and $PdCl_2$ were used as W and Pd sources, respectively. The starting solution was prepared by adding H_2WO_4 to 10 mL NaOH, which resulted in a yellow color solution, due to proton exchange process. A proper amount of $PdCl_2.2H_2O$ in 0, 5 and 10 wt% deionized water was added to the above solution. The solution pH was adjusted to 2, with the addition of 2 mL HCl. The dropping rate had to be well controlled for achieving chemical homogeneity. Then, 5 mL distilled water were added, to obtain a MWI quick response with the starting solution. The resulting precipitate was transferred into a teflon lined household microwave oven (2.45 GHz), under optimum power of 360 W, and irradiated for 5 min, in air. After MWI process, the resulting substance was dried in convection mode, at 100 ºC, for 5 min. Pure WO_3 Np were prepared in a similar manner, without Pd. The final prepared products were pale yellow and light grey, for pure and Pd-doped WO_3, respectively. Fig. 1 shows the flow chart representation of Pd-WO_3 Np experimental procedure synthesis.

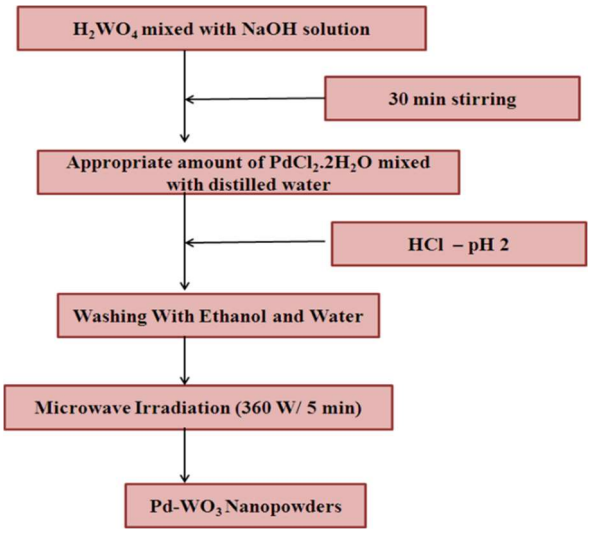

Figure 1: Flow chart representation of experimental procedure for Pd-WO_3 Np.

Results and discussion

XRD analysis

Non-destructive XRD technique was employed for categorizing Pd-doped WO_3 Np structural analysis and phase crystallinity, as shown in Fig. 2.

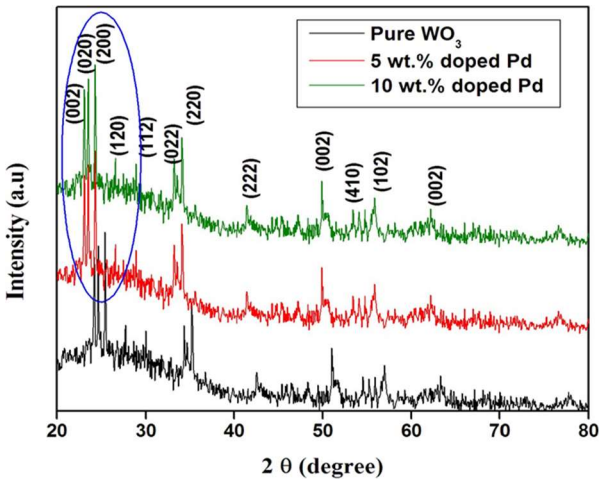

Figure 2: XRD pattern of WO_3 Np: pure; with 5 wt% Pd doping; and with 10 wt% Pd doping.

From the X- ray analysis, characteristic peaks were seen in all diffraction patterns, which were indexed to the standard card (JCPDS 83-0950). As shown in Fig. 2, all WO_3 samples have a monoclinic structure, and Pd doping did not change their crystal assemblies. No extra peaks, except for monoclinic WO_3, were seen, which can be explained by Pd species small amount and high dispersion in the samples. Moreover, the diffraction peaks of the Pd doped WO_3 samples slightly shifted towards a smaller diffraction angle than that of the pure one. Pure WO_3 lattice parameters were estimated at: a = 7.2456Å; b = 7.4324Å; c = 7.5821Å; and β = 91.001. After Pd doping, the lattice parameters decreased with higher Ct of Pd (Table 1). The difference in lattice parameters was due to Pd^{2+} ion (0.72 Å) smaller atomic radius than that of the W^{6+} ion (0.78Å).

Table 1: Lattice parameters and crystallite size of pure and Pd-doped WO_3 Np.

Ct of Pd (wt %)	Crystallite size (nm)	Lattice parameters values (A°)		
		A	B	C
0	41	7.2456	7.4324	7.5821
5	36	7.2109	7.4289	7.5729
10	28	7.1901	7.4195	7.5901

The average crystalline size of pure and Pd doped WO_3 Np was estimated using Debye Scherrer's formula, as in equation (1).

$$d = \frac{K\lambda}{\beta \cos\theta} \quad (1)$$

where d is the mean crystallite size and K is the shape factor of 0.89.

The average crystalline size of pure and 10 wt% Pd doped WO_3 was calculated as 41 and 28 nm, respectively. This result suggests that the grain growth was concealed due to Pd doping of W-site.

TEM analysis

Fig. 3 shows TEM of pure and Pd (5 and 10 wt%) doped WO_3 Np. Both pure and Pd-doped WO_3 samples clearly show mono-dispersed spherical forms with an average diameter from 50 to 30 nm, which agrees with the crystallite size estimated by XRD.

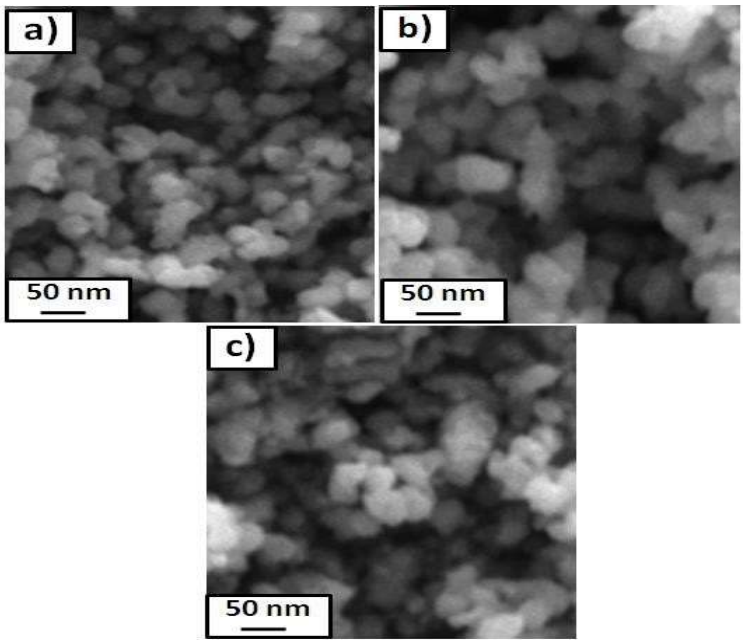

Figure 3: TEM images of WO_3 Np: **a)** pure; **b)** doped with 5 wt% Pd; and **c)** doped with 10 wt% Pd.

UV-vis TSA

In order to study the optical properties and band E_g of Pd-doped WO_3 samples, they were characterized by UV-vis TSA, as shown in Fig. 4a. In all samples, optical transparency was from 70 to 85%, but it decreased with higher Ct of Pd. Also, a significant red shift, with the increase in Ct of Pd from 0 to 10 wt%, was seen in the absorption edges, which indicates the decrease in WO_3 band E_g on doping. The absorption coefficient was calculated from TSA, using eq. (2).

$$\alpha = 1/t \ln (1/T2) \quad (2)$$

where T is optical transmission and t is the samples thickness. The direct band E_g of pure and Pd doped WO_3 samples was calculated from Fig. 4b), using eq. (3).

$$\alpha h\nu = A(h\nu - E_g)^m \quad (3)$$

where α indicates the absorption coefficient, h denotes Planck's constant, ν is incident radiation frequency and m is the factor ruling the direct or indirect movement of electrons from the valence to the conduction band.

E_g was calculated as 3.02, 2.84 and 2.73 eV, for pure, 5 and 10 wt % Pd doped

WO_3 samples, respectively (Fig. 4b). The observed decrease in E_g can be explained by the formation of intermediate energy level of pure WO_3, between valence and conduction bands, due to Pd doping.

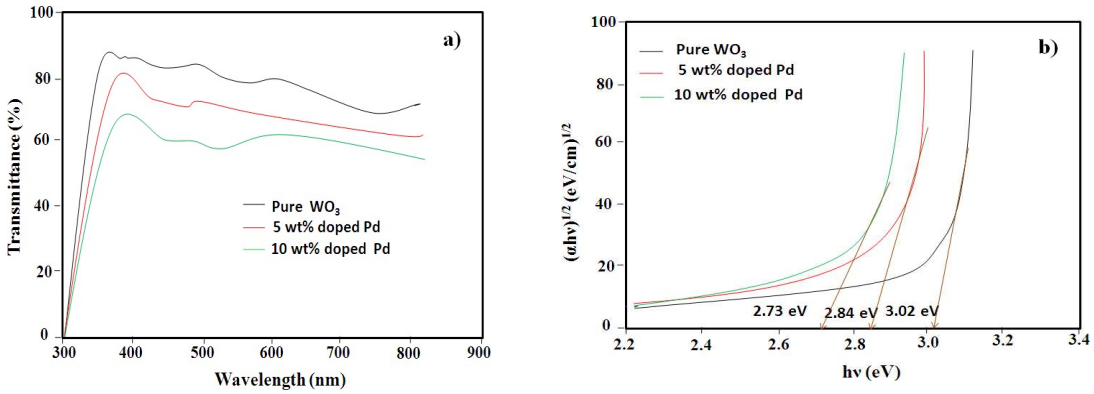

Figure 4: UV-vis spectra of WO_3 Np with different Ct of Pd. **(a)** TSA; and **(b)** E_g determination.

Pl spectra analysis

In conformity, Pl emission spectra arose from the recombination of free carriers, for all synthesized Np. Pl emission spectra of both pure and Pd doped WO_3 Np are shown in Fig. 5. They were in the range from 300 to 600 nm, using a 325 nm He-Cd laser source.

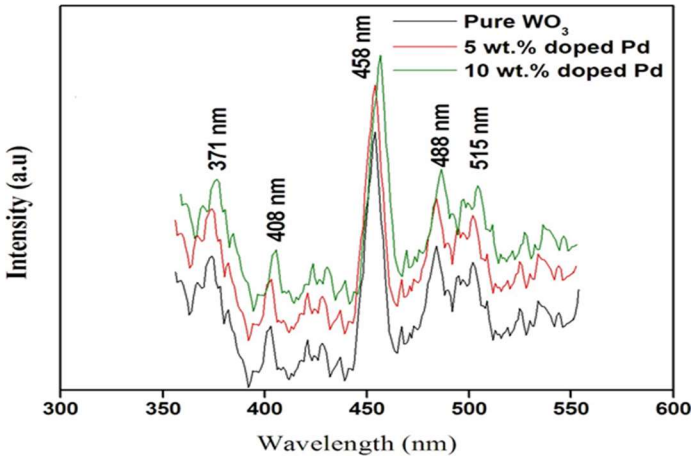

Figure 5: Pl spectra of WO_3 Np with different Ct of Pd.

The bands at 371 and 408 nm were attributed to near UV emission, due to O vacancies. These bands were caused by the localized state of O vacancies in the WO_3-x needle-like structure, as reported by [35]. A weak shoulder peak, at 458 nm, corresponds to the bluish green emission caused by defects in the samples. The green emission peak, at 515 nm, indicates V^+O vacancies. This emission was due to different Pl centers, namely, defect energy levels created by W interstitials and O vacancies. Pl intensity of the Pd-doped sample was significantly higher than that of pure WO_3, because of the recombination of photo-excited electrons and holes. Then, a lower Pl intensity (pure sample) might indicate a low recombination rate of those electrons and holes under VL irradiation.

FTIR

FTIR spectroscopy is an interesting characterization technique for analyzing the crystalline quality structure disorder and defects in Pd doped WO_3 Sc. FTIR spectra of pure and Pd-doped WO_3 Np are shown in Fig. 6. All the spectra display similar IR active modes. The bands at 615.12 cm^{-1} were due to W-O bond stretching vibrations. The region from 3000 to 3800 cm^{-1} corresponds to OH stretching vibration of the absorbed surface or internally bonded water molecules [36]. The bending mode of H-O-H was located at about 1601.23 cm^{-1}. In addition to the above bands, the small peak positioned at 131.29 cm^{-1} was associated with carbonate pieces absorption by the sample, during the annealing process [37]. No peaks were detected for Pd. This result confirmed that Pd ions substituted WO_3 site regular lattice.

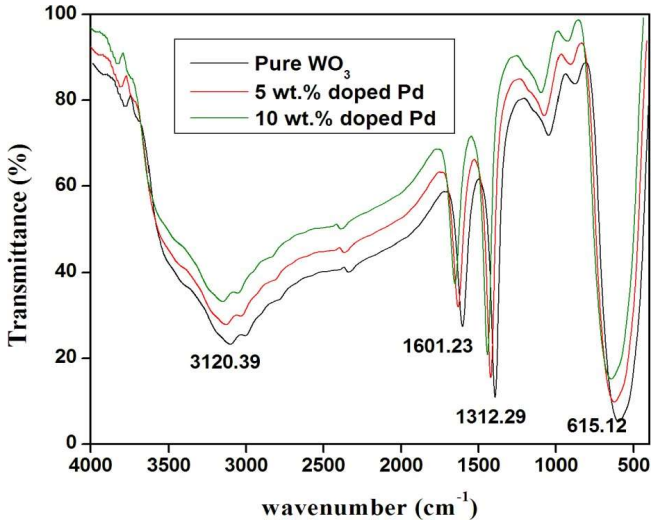

Figure 6: FTIR spectra of WO_3 Np with different Ct of Pd.

Pc activity set up

Pc activities of pure and Pd-doped WO_3 samples were evaluated by MB and RhB degradation, under VL irradiation. For the Pc process, the dyes solutions were prepared at a specific Ct (e.g. 200 mL, Ct_0 = 10 mg L^{-1}), and with a particular amount of synthesized material. A 125 W high pressure Hg lamp was used as a light source. The dyes solutions were irradiated in the horizontal direction, and the distance between the lamp and the samples was kept within 25 cm. Then, the solutions were kept in a dark room and well mixed with the magnetic stirrer, for more than 30 min, to attain equilibrium. Ct of MB and RhB in each sample were analyzed using an UV-vis spectrophotometer, at a wavelength of 664 nm. Pc efficiency was calculated from the expression given by eq. (4).

$$\eta = (1\text{-}C/C_0) \quad (4)$$

where C_0 and C are Ct of MB and RhB dyes before and after a certain irradiation time, respectively.

Pc activity measurements

Pc activities of pure and Pd-doped WO_3 samples were evaluated based on their

ability to degrade MB and RhB under VL. The findings revealed that irradiation time and Ct of Pc induced the reactive dyes degradation. Figs. 7 and 8 show the catalyst effect Ct on MB and RhB degradation profiles under VL irradiation. In both cases, the degradation was linearly increased with higher Ct of Pd. Particularly, the significant improvement in degradation was observed in the Pd-doped WO_3 catalyst. After 120 min, MB degradation was 56, 73 and 84%, for pure and Pd (5 and 10 wt%) doped WO_3 samples, respectively.

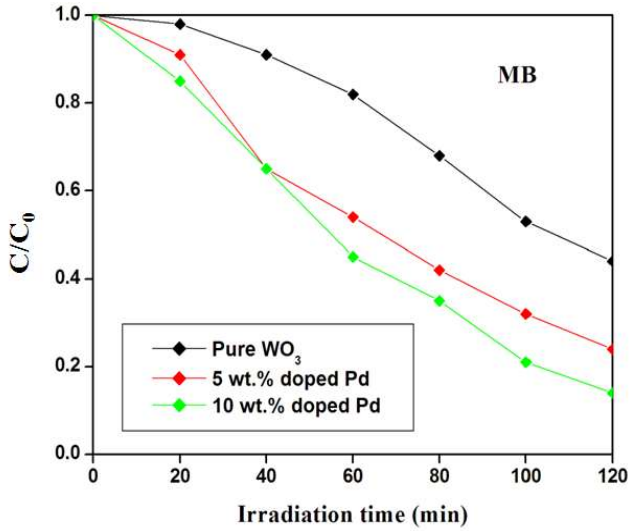

Figure 7: Pc degradation of MB using Pd-WO_3 under VL irradiation.

Similarly, pure, 5 and 10 wt% Pd doped WO_3 samples degradation efficiency of RhB was about 59, 78 and 92%, respectively. The significant improvement in the Pc performance was due to an increase in SA, as well as to O vacancies created by Pd doping. In addition, lower E_g was another crucial factor that increased Pc efficiency. Sequentially, the catalyst was subject to multiple cycles under the same procedure, for confirming that it was stable and reusable.

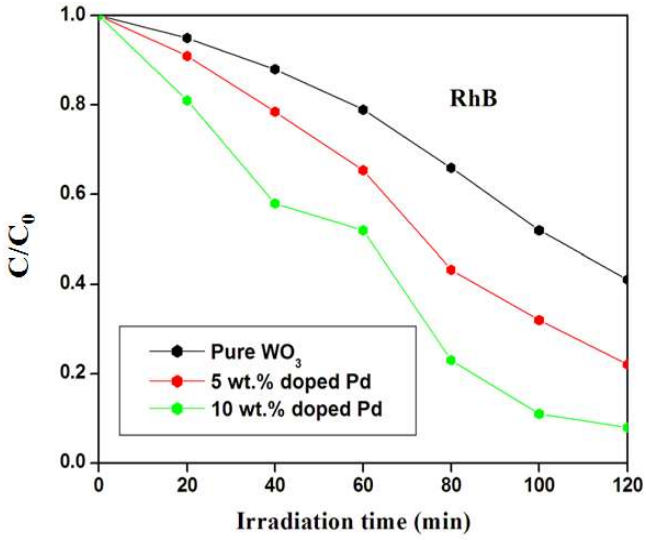

Figure 8: RhB Pc degradation using Pd-WO_3 under VL irradiation.

Fig. 9 shows the seven runs of RhB photo degradation by using Pd (10 wt%) doped WO_3 Pc. The result shows the slight variation in the decolorization/degeneration, due to incomplete recollection and loss during the washing process.

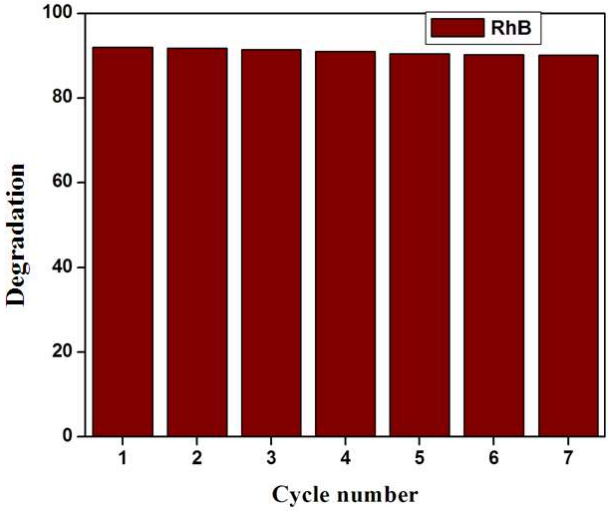

Figure 9: Seven cycles of RhB degradation using Pd-WO_3 as Pc.

Fig. 10 shows the schematic representation of the Pc mechanism for RhB discoloration. One possible reason for the high SA and O vacancies of the Pd-WO_3 Pc may be Active $^{\bullet}OH$ generation. Active •OH radicals were produced on the Pc surface by the reaction of photo generated h^+vb holes and adsorbed OH^-. Other reason may be that the smaller E_g of Pd-WO_3 catalyst (2.56 eV) allowed OH^- oxidization to active OH [38], which is the primary oxidizing species in Pc processes. Therefore, higher Ct of OH^- and, thus, increased Pc generation of active $^{\bullet}OH$, from the Pd-WO_3 surface, enhanced MB and RhB discoloration.

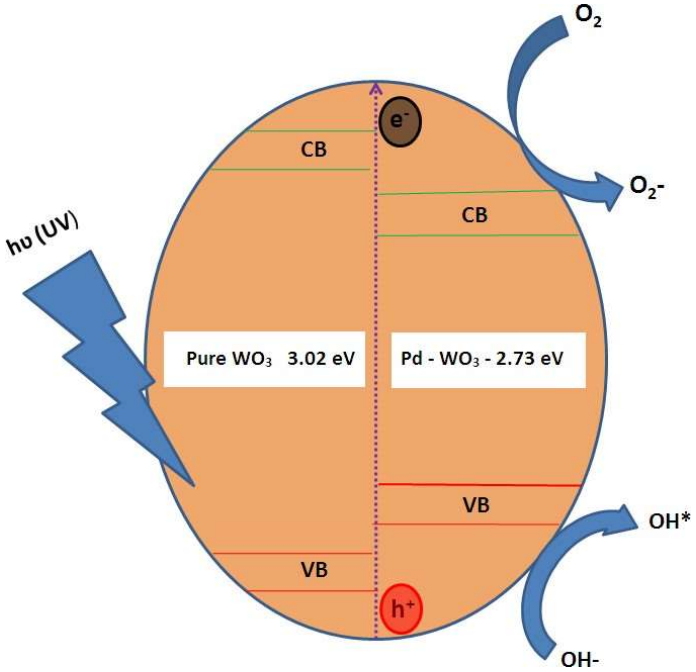

Figure 10: Schematic representation of Pd-WO_3 Pc mechanism for RhB.

Conclusion

In this study, pure and Pd-doped WO_3 Pc NP were admirably synthesized from $PdCl_2.2H_2O$ precursors by MWI method. XRD and TEM results suggest that the Pd dopant did not influence WO_3 structure and morphology, but it reduced its grain size. UV-vis and Pl studies showed that pure WO_3 optical properties were significantly improved by Pd doping. The obtained materials were used as Pc for MB and RhB discoloration under VL irradiation. Pd-doped WO_3 showed higher Pc activity than that of the pure one. Greatly improved Pc activity of Pd doped WO_3 indicates that the smaller E_g, the smaller particle size, and also the higher SA.

Acknowledgement

M. Sangeetha wishes to state his deep sense of gratitude and profound thanks to his research supervisor Dr. P. Rajkumar, assistant professor, at the Department of Physics, Government Arts College, Kulithalai, for his keen interest, inspiring guidance, constant encouragement with his work during all stages, in order to bring this study into fruition. He owes his loving thanks to his parents Mr. K. Dhandapani and Mrs. D. Sakunthala, his brother Mr. D. Parthian, his wife Dr. M. Sangeetha, and his daughter S. M. Karnega Priyal, for their endless love, encouragement and support.

Authors' contribution

D. Madhan: conceived the original idea; collected data; developed the theory; designed and carried out the experiment; inserted data; performed calculations; wrote the manuscript with support from authors. **M. Sangeetha:** contributed to the sample preparation; verified the analysis methods, formulas and calculations; contributed to the results interpretation; contributed to the manuscript writing. **A. Panneerselvam**: contributed to the manuscript design and writing; supervised the findings of this work; provided critical feedback; helped to shape the research, analysis and manuscript.

Abbreviations

Ct: concentration
E_g: band gap energy
FTIR: Fourier transform infrared
H_2WO_4: tungstic acid
h^+vb: valence band holes
JCPDS: Joint Committee on Powder Diffraction Standards
MB: methylene blue
MWI: microwave irradiation
NaOH: sodium hydroxide
Np: nanoparticles
$^{\bullet}OH$: hydroxyl radicals
OH^-: hydroxyl anions
Pc: photocatalytic/photocatalyst
$PdCl_2.2H_2O$: palladium chloride dihydrate
Pl: photoluminescence

RhB: rhodamine B
SA: surface area
Sc: semiconductor
TEM: transmission electron microscopy
TSA: transmission spectra analysis
UV-vis: visible ultraviolet
VL: visible light
WO_3: tungsten trioxide
$WO_3.H_2O$: tungstite
XRD: X-ray diffraction

Symbols definition
β: full width half maximum
η: order of diffraction
θ: Bragg's reflection angle in degree
λ: wavelength of the incident beam
ν: frequency of incident light

References

1. Lavacchi A, Bellini M, Berretti E et al. Titanium dioxide nanomaterials in electrocatalysis for energy. Curr Opin Electrochem. 2021;28:100720. https://doi.org/10.1016/j.coelec.2021.100720
2. Mesgari M, Aalami AH, Sahebkar A. Antimicrobial activities of chitosan/titanium dioxide composites as a biological nanolayer for food preservation: A review. Int Bio Macromolec. 2021;176:530-539. https://doi.org/10.1016/j.ijbiomac.2021.02.099
3. Abazari R, Mahjoub AR, Saghatforoush LA et al. Characterization and optical properties of spherical WO3 nanoparticles synthesized via the reverse microemulsion process and their photocatalytic behavior. Mat Lett. 2014;133:208-211. https://doi.org/10.1016/j.matlet.2014.07.032
4. Linsebigler AL, Lu G, John T et al. Photocatalysis on TiO2 surfaces: Principles, mechanisms, and Selected Results. Chem Rev. 1995; 95:735-758. https://doi.org/10.1021/cr00035a013
5. Fujishima A, Zhang X, Tryk DA. TiO2 photocatalysis and related surface phenomena. Surf Sci Rep. 2008;63:515-582. https://doi.org/10.1016/j.surfrep.2008.10.001
6. Han C, Yang MQ, Weng B et al. Improving the photocatalytic activity and anti-photocorrosion of semiconductor ZnO by coupling with versatile carbon. Phys Chem Chem Phys. 2014;16:16891-16903. https://doi.org/10.1039/C4CP02189D
7. Weng B, Liu S, Tang ZR et al. One-dimensional nanostructure based materials for versatile photocatalytic applications. RSC Adv. 2014;25:12685-12700. https://doi.org/10.1039/C3RA47910B
8. Jana R, Pathak TP, Sigman MS. Advances in transition metal (Pd, Ni, Fe)-catalyzed cross-coupling reactions using alkyl-organometallics as reaction partners. Chem Rev. 2011;111:1417-14923. https://doi.org/10.1021/cr100327p
9. Mills A, Le Hunte S. An overview of semiconductor photocatalysis. J Photochem Photobiol A: Chem. 1997;108:01-35. https://doi.org/10.1016/S1010-6030(97)00118-4
10. Rafatullah M, Sulaiman O, Hashim R, Ahmad, A. Adsorption of methylene blue on low-cost adsorbents: A review. J Hazard Mat. 2010;177:70-80. https://doi.org/10.1016/j.jhazmat.2009.12.047

11. Derakhshan Z, Baghapour MA, Ranjbar M et al. Adsorption of Methylene Blue Dye from Aqueous Solutions by Modified Pumice Stone: Kinetics and Equilibrium Studies. Health Scope. 2013;2:136-144. https:// 10.17795/jhealthscope-12492
12. Dutta K, Mukhopadhyay S, Bhattacharjee S et al. Chemical oxidation of methylene blue using a Fenton-like reaction: J Hazard Mat. 2001;84:57-71. https://10.1016/s0304-3894(01)00202-3
13. Konstantinou IK, Albanis TA. TiO_2-Assisted Photocatalytic Degradation of Azo Dyes in Aqueous Solution: Kinetic and mechanistic investigations: A Review. Appl Catal B: Environ. 2004;49:1-14. https://doi.org/10.1016/j.apcatb.2003.11.010
14. Melghit K, Al-Rubaei MS, Amri IA. Photodegradation enhancement of Congo red aqueous solution using a mixture of $SnO2{\cdot}xH_2O$ gel/ZnO powder. J Photochem Photobiol A: Chem. 2006;181:137-141, https://doi.org/10.1016/j.jphotochem.2005.11.015
15. Peng Y, Liu C, Zhang X et al. The effect of SiO2 on a novel CeO2–WO3/TiO2 catalyst for the selective catalytic reduction of NO with NH3. Appl Catal B: Environ. 2013;140-141:276-282. https://doi.org/10.1016/j.apcatb.2013.04.030
16. Zhang L, Tang X, Lu Z et al. Facile synthesis and photocatalytic activity of hierarchical WO_3 core–shell microspheres. Appl Surf Sci. 2011;258:1719-1724. https://doi.org/10.1016/j.apsusc.2011.10.022
17. Osai Ai, Takashi O, Asep BDN et al. Controllable crystallite and particle sizes of WO3 particles prepared by a spray-pyrolysis method and their photocatalytic activity. AIChE J. 2013;60:41-49. https://doi.org/10.1002/aic.14233
18. Phuruangrat A, Ham DJ, Hong SJ et al. Synthesis of hexagonal WO_3 nanowires by microwave-assisted hydrothermal method and their electrocatalytic activities for hydrogen evolution reaction. J Mat Chem. 2010;20:1683-1690. https://doi.org/10.1039/B918783A
19. Hua Z, Yuasa M, Kida T et al. High sensitive gas sensor based on Pd-loaded WO3 nanolamellae. Thin Solid Films. 2013;548:677-682. https://doi.org/10.1016/j.tsf.2013.04.088
20. Bai X, Ji,H, Gao P et al. Morphology, phase structure and acetone sensitive properties of copper-doped tungsten oxide sensors. Sens Actuat B: Chem. 2014;193:100-106. https://doi.org/10.1016/j.snb.2013.11.059
21. Upadhyay SB, Mishra RK, Sahay PP. Structural and alcoholresponse characteristics of Sn-doped WO_3 nanosheets. Sens Actuat B: Chem. 2014;193:19-27. https://doi.org/10.1016/j.snb.2013.11.049
22. Aramendia MA, Borau V, Colmenares JC et al. Modification of the photocatalytic activity of Pd/TiO_2 and Zn/TiO_2 systems through different oxidative and reductive calcination treatments. Appl Catal B: Environ. 2008;80:88-97. https://doi.org/10.1016/j.apcatb.2007.11.017
23. Seki T, Grunwaldt JD, Vegten NV et al. Palladium Supported on an Acidic Resin: A Unique Bifunctional Catalyst for the Continuous Catalytic Hydrogenation of Organic Compounds in Supercritical Carbon Dioxide. Adv Synth Catal. 2008;350:691-705. https://doi.org/10.1002/adsc.200700532
24. Singh UG, Li J, Bennett JW et al. A Pd-doped perovskite catalyst, $BaCe_1{-}xPdxO_3{-}\delta$, for CO oxidation. J Catal. 20074;249:349-358. https://doi.org/10.1016/j.jcat.2007.04.023
25. Liewhiran C, Phanichphant S. Effects of Palladium Loading on the Response of Thick Film Flame-made ZnO Gas Sensor for Detection of Ethanol Vapor. Sensors. 2007;7:1159-1184. https://doi.org/10.3390/s7071159

26. Vaishampayan MV, Deshmukh RG, Mulla IS. Influence of Pd doping on morphology and LPG response of SnO_2. Sens Actua B: Chem. 2008;131:665672. https://doi.org/10.1016/j.snb.2007.12.055
27. Elias Burstein. Anomalous Optical Absorption Limit in InSb. Phys Rev. 1954; 93:632-633. https://doi.org/10.1103/PhysRev.93.632
28. Moss TS. The Interpretation of the Properties of Indium Antimonide. Proceed Phys Soc. Sec B. 1954;67:775-782. https://iopscience.iop.org/article/10.1088/0370-1301/67/10/306/pdf
29. Shan FK, Kim BI, Liu GX et al. Blue shift of near band edge emission in Mg doped ZnO thin films and aging. J Appl Phys. 2004;95:4772-4776. https://doi.org/10.1063/1.1690091
30. Singh MR. Transparency and spontaneous emission in a densely doped photonic band gap material. J Phys B: Atom, Molec Optic Phys. 2006;39:5131-5142. https://iopscience.iop.org/article/10.1088/0953-4075/39/24/010
31. Cong W, CAO L. Preparation, spectral characteristics and photocatalytic activity of Eu^{3+}-doped WO_3 nanoparticles. J Rare Earths. 2011;29:727- 731. https://doi.org/10.1016/S1002-0721(10)60531-5
32. Hariharan V, Parthibavarman M, Sekar C. Synthesis of tungsten oxide (W18O49) nano sheets utilizing EDTA salt by microwave irradiation method. J Allo Comp. 2011;509:4788-4792. https://doi.org/10.1016/j.jallcom.2011.01.159
33. Ha JH, Muralidharan P, Kim DK. Hydrothermal synthesis and characterization of self-assembled h-WO3nanowires/nanorods using EDTA salts. J Allo Comp. 2009;475:446-451. https://doi.org/10.1016/j.jallcom.2008.07.048
34. Asim N, Radiman S, Yarmo MAB. Preparation of WO3 Nanoparticles Using Cetyl Trimethyl Ammonium Bromide Supermolecular Template. American j Appl Sci. 2009;6:1424- 1428. https://doi.org/10.3844/ajassp.2009.1424.1428
35. Wang Y, Zhang L, Meng G et al. Zn Nanobelts: a new quasi one-dimensional metal nanostructure. Chem Commun. 2001;24:2632-2633. https://doi.org/10.1039/B108158F
36. Pang C, Luo J, Guo Z et al. Inhibition of tungsten particle growth during reduction of V-doped WO3 nanoparticles prepared by co-precipitation method. Int J Refrac Met Hard Mat. 2010;28:343-348. https://doi.org/10.1016/j.ijrmhm.2009.11.010
37. Kida T, Nishiyama A, Yuasa M et al. Highly sensitive NO_2 sensors using lamellar-structured WO_3 particles prepared by an acidification method. Sens Actua B: Chem. 2009;135:568-574. https://doi.org/10.1016/j.snb.2008.09.056
38. Deepa M, Kar M, Singh DP et al. Influence of polyethylene glycol template on microstructure and electrochromic properties of tungsten oxide. Solar Ener Mat Solar Cells. 2008;92:170-178. https://doi.org/10.1016/j.solmat.2007.01.024
39. Madhan D, Parthibavarman M, Rajkumar P et al. Influence of Zn doping on structural, optical and photocatalytic activity of WO_3 nanoparticles by a novel microwave irradiation technique. J Mat Sci: Mat Electron. 2015;26:68236830. https://doi.org/10.1007/s10854-015-3296-5